The model parameters

$$\hat{\boldsymbol{\Theta}}^T = \left[\hat{\boldsymbol{\Theta}}_1^T, \hat{\boldsymbol{\Theta}}_2^T, \hat{\boldsymbol{\Theta}}_3^T, \hat{\boldsymbol{\Theta}}_4^T\right] \tag{6.1.38}$$

were estimated by the least-squares method in the form of discrete square-root filtering (DSFI). Based on the model parameter estimates $\hat{\boldsymbol{\Theta}}$ all nine process coefficients of $\mathbf{p}$ could be calculated uniquely.

The DC motor is controlled by an AC/DC converter with cascade control of the speed and the armature current as auxiliary control variable. The manipulated variable is the armature current U_2. A microcomputer DEC-LSI 11/23 was connected online to the process. For the experiments the reference value $W(t)$ of the speed control has been changed stepwise with a magnitude of 750 rpm every 2 min. The operating point was $n = 1000\,\text{rpm}$, $H = 5.4\,\text{m}$ and $\dot{V} = 6.48\,\text{m}^3/\text{h}$. The signals were sampled with sampling time $T_0 = 5\,\text{ms}$ and 20 ms over a period of 2.5 and 10 s, so that 500 samplings were obtained. These measurements were stored in the core memory before estimation. Hence, one set of parameters and process coefficients was obtained every 120 s. For the training phase 50 coefficient sets were used. Table 6.4 gives an overview of significant changes of process coefficients for 19 different artificially generated faults. A selection of experiments will now be considered in more detail.

1) *Fault A5*: *Disturbance of the air cooling of the DC motor*, Figure 6.10
   A stepwise reduction (20%, 50%, 75%, 100%) of the air flow (e.g. due to plugging by dirt) leads to a temperature change of the whole motor and therefore to an increase of the resistance in the armature circuit and excitation circuit. Therefore, R_2 increases and the magnetic flux linkage Ψ decreases. This is an example where the coefficients move in opposite directions.
2) *Fault P3*: *Increase of slot clearance of the centrifugal pump*, Figure 6.11
   An increase of the slot clearance between the pump wheel and the pump case increases the internal losses. Therefore, h_{th1} increases and h'_{nn} decreases.
3) *Fault F1a*: *Cavitation in the centrifugal pump*, Figure 6.12
   A small cavitation and gas bubble generation in the pump by lowering the entrance pressure is indicated by an increasing coefficient a_F, which is proportional to the time constant of the pipe system, see (6.1.13).

These experiments have demonstrated that in all cases, where a significant change of process coefficients could be expected the fault could be detected. Based on the patterns given in Table 6.4 most of the faults can be isolated. At least motor faults are clearly isolable from pump faults.

6.1.4 Fault detection with nonlinear parity equations and parameter estimation

In order to develop an online fault detection and diagnosis method for a centrifugal pump–pipe–tank system over a large operating range, a plant according to Figures 6.13 and 6.14 is considered. The pump is driven by an inverter-fed, speed-variable induction (squirrel-cage) motor which is speed-controlled by a field-oriented controller. The stator current vector $\mathbf{I}_s = I_{s\alpha} + i\,I_{s\beta}$ is measured and transformed in the

Table 6.4. Detected symptoms for the DC motor and centrifugal pump based on parameter estimation for stepwise speed changes. +: positive change, −: negative change, 0: no change

Fault	Symptom								
	L_2	R_2	Ψ	J_P	M_{f0}	h_{th1}	h'_{nn}	a_F	h_{rr}
A1: exc. resistance increase	0	0	−	0	0	0	0	0	0
A2: armature resistance increase	0	+	−	0	0	0	0	0	0
A3: affected brushes	−	+	−	0	0	0	0	0	0
A4: new brushes	0	0	0	0	0	0	0	0	0
A5: insufficient cooling	0	+	−	0	0	0	0	0	0
A6: cold drive	0	0	+	−	0	0	0	0	0
K1: shaft displacement	0	0	0	−	0	0	0	0	0
P1a: bearing without grease	0	0	0	0	−	0	0	0	0
P1b: bearing with dirt	0	0	0	+	+	+	0	0	0
P2: side thrust compensation defective	0	0	0	0	0	0	0	0	0
P3: splitting clearance increase	0	0	0	0	0	+	−	0	0
P4: affected impeller	0	0	0	−	0	+	−	0	0
P5a: pump casing defective I	0	0	0	0	+	0	0	0	0
P5b: pump casing defective II	0	0	0	0	−	+	0	+	0
F1a: little cavitation	0	0	0	0	0	0	0	+	0
F1b: medium cavitation	0	0	0	0	0	+	−	+	−
F2: insufficient venting	0	0	0	0	0	+	−	−	−
F3: fluid temperature increase	0	0	0	0	0	0	−	0	−
F4: valve position increase	0	0	0	0	0	+	0	0	+

reference frame defined by the rotor flux $\mathbf{I}_s = I_{sd} + i\,I_{sq}$ which is obtained by using an adequate model, see Section 3.2.

The motor torque can then be determined by

$$M_{mot} = k_T \Psi_R I_{sq} \tag{6.1.39}$$

where k_T is known from the motor data sheet.

Further measurements are:

p_1 pump pressure inlet
p_2 pump pressure outlet
ω pump speed
$\dot{V}$ volume flow.

Figure 6.15 shows the overall configuration of the investigated pump–pipe system. The mathematical models of the pump used have to be adapted to the pump–pipe system, [6.5], [6.30]. Based on the theoretically derived equations from Section 6.1.2 the following models are used here:

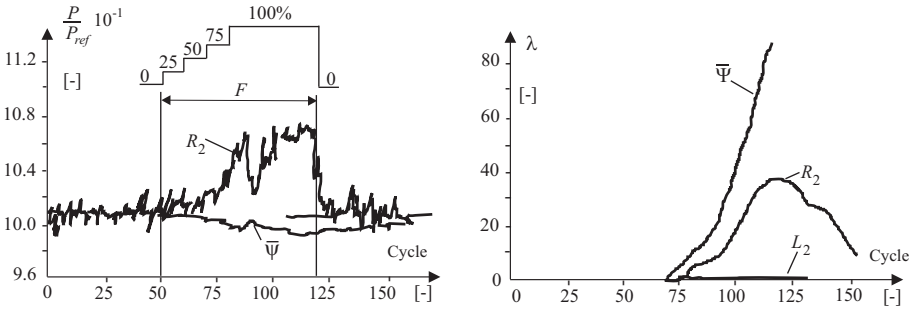

Fig. 6.10. Change of process coefficients for reduction of the cooling air flow. (λ) is the test quantity of a Bayes decision test, [6.6]

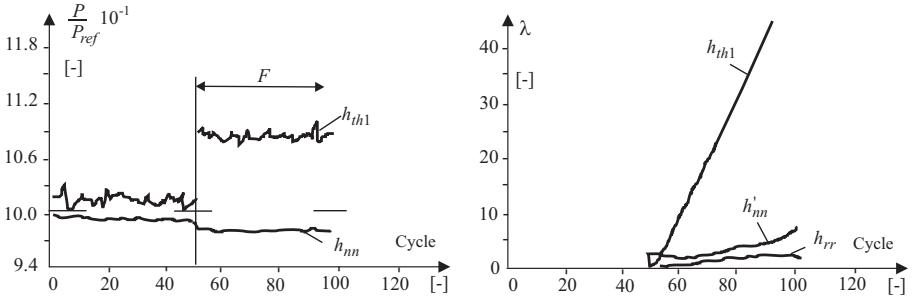

Fig. 6.11. Change of process coefficients after increasing the slot clearance of the pump

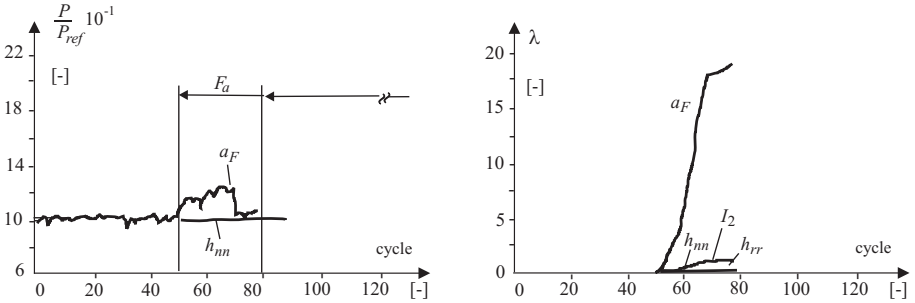

Fig. 6.12. Change of process coefficients in the case of small cavitation and gas bubble generation in the pump

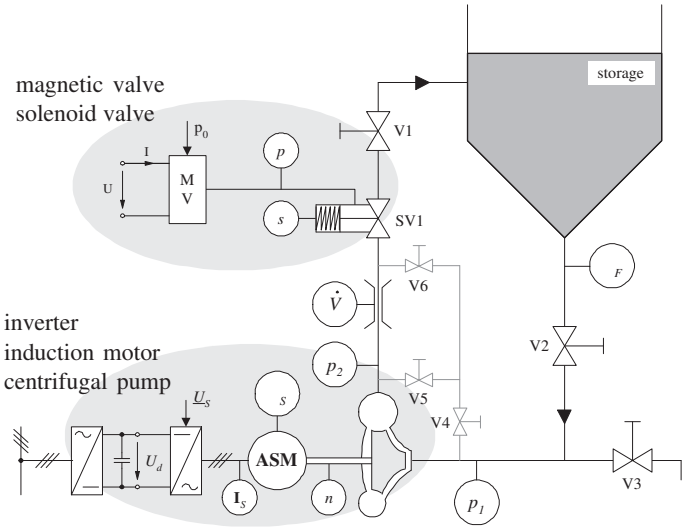

Fig. 6.13. Centrifugal pump–pipe–tank plant with measurements: AC motor: Siemens 1 LA 5090-2AA (norm motor) $P_N = 1.5\,\text{kW}$; $n_W = 2900\,\text{rpm}$; frequency converter: Lust MC 7404; circular pump: Hilge, $H_{max} = 130\,\text{m}$; $\dot{V}_{max} = 14\,\text{m}^3/\text{h}$; $P_{max} = 5.5\,\text{kW}$

Fig. 6.14. Photo of the investigated centrifugal pump–pipe–tank plant

$$H(t) = h_{nn}\omega^2(t) - h_{nv}\omega(t)\dot{V}(t) - h_{vv}\dot{V}^2(t) \tag{6.1.40}$$

$$H(t) = \frac{p_2(t) - p_1(t)}{\rho g} = \frac{\Delta p(t)}{\rho g} \tag{6.1.41}$$

$$H(t) = a_F d\dot{V}(t)/dt + h_{rr}\dot{V}^2(t) \tag{6.1.42}$$

$$J_p\dot{\omega}(t) = M_{mot}(t) - M_{th}(t) - M_f(t) \tag{6.1.43}$$

$$M_{th}(t) = M_{th1}\omega(t)\dot{V}(t) - M_{th2}\dot{V}^2(t) \tag{6.1.44}$$

$$M_f(t) = M_{f0}\ \text{sign}\ \omega(t) + M_{f1}\omega(t) \tag{6.1.45}$$

A comparison of these theoretically derived equations has shown that because of (6.1.11), neglect of the viscous friction in (6.1.32) and (6.1.8), the following simplified relations can be used, [6.30]:

$$\Delta p(t) = \tilde{h}_{nn}\omega^2(t) - \tilde{h}_{\omega}\omega(t) \tag{6.1.46}$$

$$J_P\dot{\omega}(t) = M_{mot}(t) - M_{f0}(t) - M_2\omega^2(t) \tag{6.1.47}$$

These models agree also with a larger pump–pipe system, [6.5]. Figure 6.16 shows the resulting signal flow diagram.

a) Measurement of $I, \omega, \Delta p, \dot{V}$

Based on these models and after discretizing, the following residuals can be obtained, compare Figure 6.17 and [6.30], [6.32]:

Static pump model (6.1.46):

$$r_1(k) = \Delta p(k) - w_1\omega^2(k) + w_2\omega(k) \tag{6.1.48}$$

Dynamic pipe model (6.1.42):

$$r_2(k) = \dot{V}(k) - w_3 - w_4\sqrt{\Delta\hat{p}(k)} - w_5\dot{V}(k-1) \tag{6.1.49}$$

Dynamic pump–pipe model (6.1.42), (6.1.46)

$$r_3(k) = \dot{V}(k) - w_3 - w_4\sqrt{\Delta\hat{p}(k)} - w_5\dot{V}(k-1) \tag{6.1.50}$$

$$\Delta\hat{p}(k) = w_1\omega^2(k) - w_2\omega(k) \tag{6.1.51}$$

Dynamic inverse pump model (6.1.48)

$$r_4(k) = M_{mot}(k) - w_6 - w_7\omega(k) - w_8\omega(k-1) - w_9\omega^2(k) - w_{10}M_{el}(k-1) \tag{6.1.52}$$

The residuals $r_1(k)$), $r_2(k)$ and $r_3(k)$ are output residuals which follow by comparing the measured $\Delta p(k)$ and $\dot{V}(k)$ with the corresponding model outputs, see Figure 6.17. However, $r_4(k)$ is an input residual, because $M_{mot}(k)$ is compared with the output of an inverse pump model. $r_2(k)$ and $r_3(k)$ include flow sensor dynamics of first order. The sampling time is $T_0 = 10$ ms.

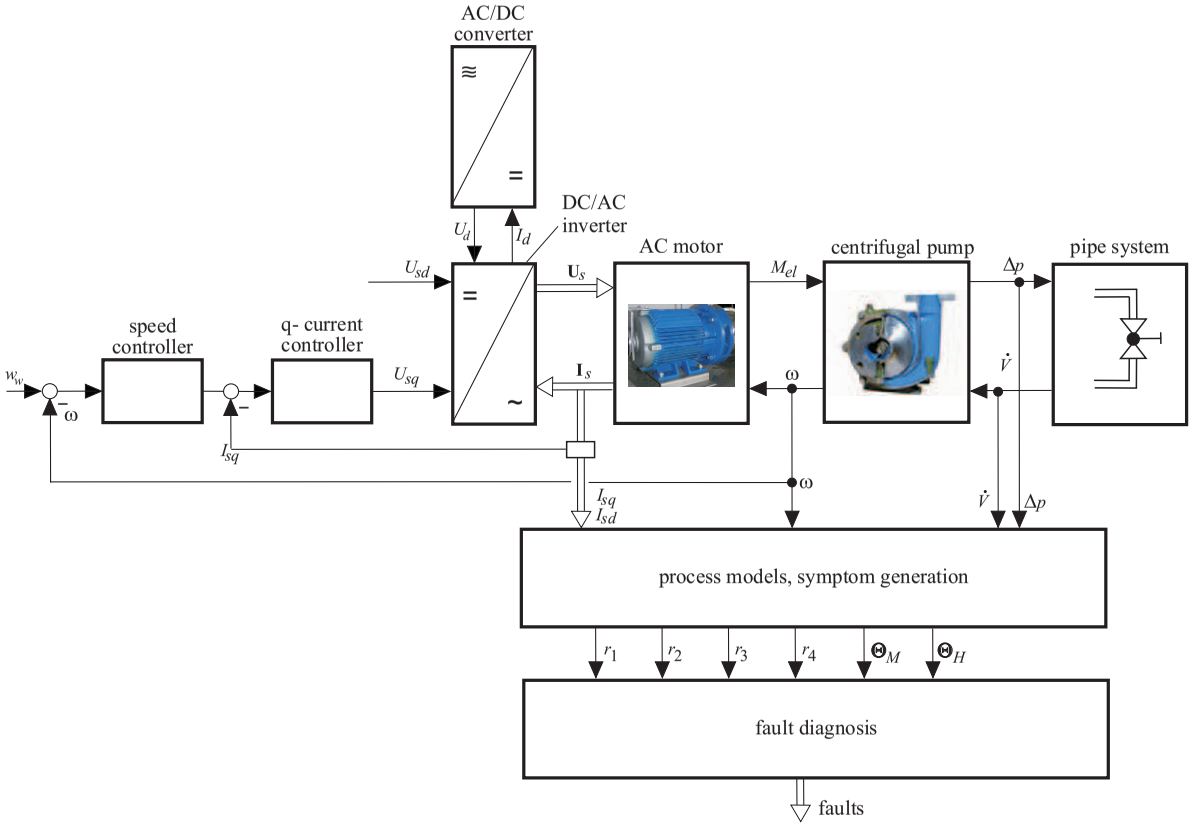

Fig. 6.15. Scheme of the model-based fault detection and diagnosis system for a speed-controlled centrifugal pump with parity equations and parameter estimation. $\mathbf{U}_s$: pulse-width-modulated stator voltage vector; $\mathbf{I}_s$: stator current vector

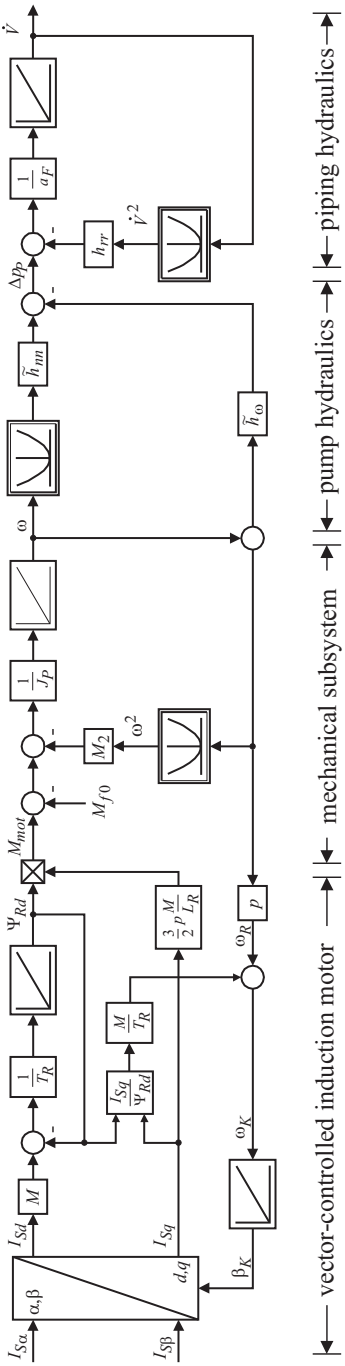

Fig. 6.16. Signal flow diagram of the simplified nonlinear overall motor–pump–pipe system

The parameters $w_1, \ldots, w_{10}$ follow directly from known physical data described in the equations above or are estimated, e.g. with methods of least squares based on measurements of $I_{sq}(t)$, $\omega(t)$, $\Delta p(t)$ and $\dot{V}(t)$. However, the parameters w_i depend, especially for low speed at the operating point. Therefore, for each residual a multi-model approach is used. It has turned out that it is sufficient to consider the parameters dependent on the angular speed only.

The pump system was excited by changing the speed according to an amplitude-modulated PRBS over the whole operating range, and with the local linear model network LOLIMOT the parameters $w_i(\omega), i = 1, \ldots, 10$ were determined using three local models each, see [6.15]. Figure 6.18 shows a comparison of measured and reconstructed values with the models. Hence, a very good agreement can be stated.

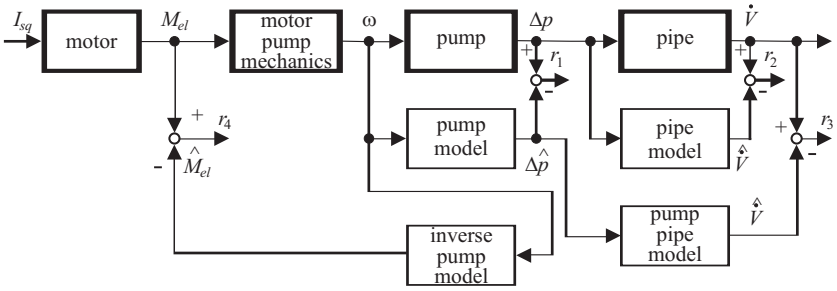

Fig. 6.17. Residual generation with parity equations for the pump–pipe system

The following faults were introduced into the pump–pipe system:

- Offset sensor faults ω, $\dot{V}$, p_1, p_2
- Increased resistance by piecewise closing of a valve after the pump
- Cavitation by piecewise closing of a valve before the pump
- Increased bearing friction by removing grease and introducing iron deposits
- Impeller defect by closing one channel between two vanes with silicon
- Sealing-gap losses by opening a bypass valve
- Leakage between pump and flow measurement.

Table 6.5 shows the resulting symptoms. The residuals of the parity equations can be obtained without input excitation, i.e. in steady-state operation. The resulting residuals indicate that the sensor offset faults, sealing-gap losses and increased bearing friction are strongly isolable. However, increased flow resistance, cavitation and impeller defect are either only weakly or not isolable. This means that all the faults are detectable but some of them cannot be differentiated. As in the case of dynamic excitation the nonlinear models are very precise, passing deviations of the residuals result. In order to avoid over-large thresholds, adaptive thresholds are used. In addition to a constant value, the thresholds depend on a high-pass-filtered value of the speed ω, which increases the threshold in the case of a speed change, [6.30], [6.31].

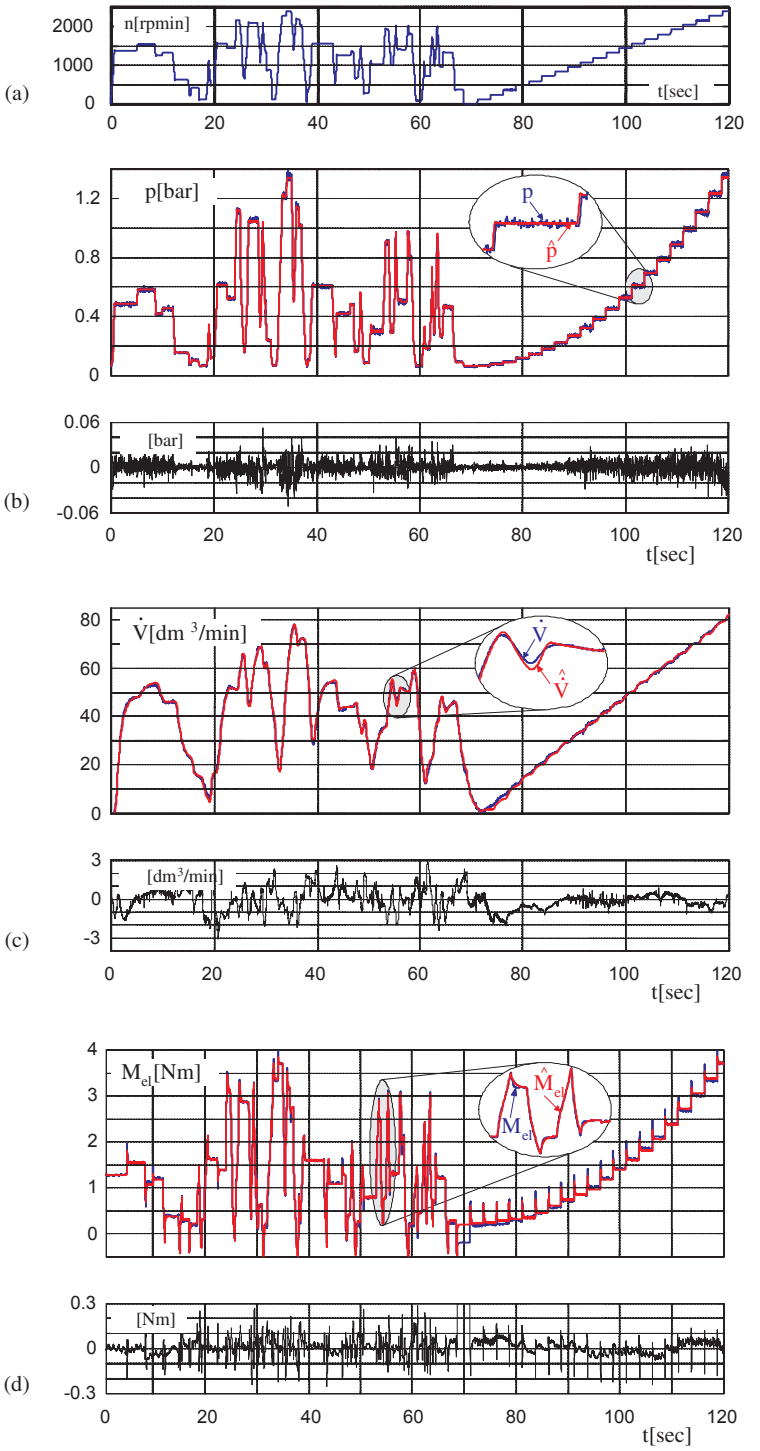

Fig. 6.18. Measured signals of the pump–pipe system, LOLIMOT model outputs and their differences: a) angular speed; b) delivery pressure difference; c) flow rate; d) torque of AC motor

A dynamic excitation with a test PRBS for the speed also allows one to estimate the parameters of the models (6.1.42), (6.1.46) and (6.1.47) with a recursive least-squares method as described in Section 2.5, see also [6.13], Section 2.5. The changes of these physically defined parameters are given in Table 6.5 and show that now all faults are isolable and can therefore be diagnosed by combining the two methods.

b) Measurement of I, ω

If the delivery pressure Δp and the flow rate $\dot{V}$ are not measurable, the residual r_4 can be calculated based on measured speed ω and motor current I_{sq}. This allows one to detect a sensor fault in ω and some pump faults. Additional parameter estimation enables one to determine parameter deviations of J_P, M_{f0} and M_2 with (6.1.47) and to isolate some more pump faults.

Similar results as described above have been obtained by [6.5] for a larger pump with $P = 3.3\,\text{kW}$ and $\dot{V}_{max} = 150\,\text{m}^3/\text{h}$ and a larger pipe circulation system with two heat exchangers. Two different flow meters could be used. This allowed the generation of six residuals and four parameter estimates. Together with two variances of residuals, altogether 13 symptoms could be obtained, which enabled the diagnosis of 11 different faults of sensors, pump and pipe system.

These symptoms were then used to train 20 fuzzy rules with the SELECT procedure described in [6.15], Section 17.3.5, yielding a 100% classification accuracy.

Table 6.6 enables one to see which faults are only detectable or also diagnosable with combined parity equations and parameter estimation. A minimal measurement of the torque $M = f(I)$ and speed ω allows one to detect some few faults but not to diagnose them. By adding a sensor for p_1 and p_2, or for Δp, many more faults can be detected and diagnosed. The additional implementation of a flow rate sensor has little influence on the number of detectable faults, but allows one to diagnose many more faults. This shows that model-based detection of faults is possible with three to four sensors, but that the fault diagnosis is improved considerably by one additional sensor (here the flow rate).

6.1.5 Fault detection with vibration sensors

Rotating machinery such as centrifugal and reciprocating pumps generates certain oscillations. In the case of centrifugal pumps these oscillations are generated by the rotating shafts, blades of the rotors, ball bearings, unbalance and fluid oscillations through turbulence and vortex or cavitation. The arising frequencies therefore depend on the rotational speed, flow rate and special fluid-phenomena.

Therefore is is obvious to detect changes, malfunctions and faults through vibration and oscillation measurements, especially also as some faults can be detected by the human ear. The available sensors are, e.g. oscillation velocity sensors with a low-frequency suspended seismic mass and inductively generated voltage or oscillation accelerometers with a high-frequency suspended seismic mass or with piezoelectrical sensors possessing small mass and large spring stiffness.

http://www.springer.com/978-3-642-12766-3

Fault-Diagnosis Applications
Model-Based Condition Monitoring: Actuators, Drives, Machinery, Plants, Sensors, and Fault-tolerant Systems
Isermann, R.
2011, XVI, 354 p., Hardcover
ISBN: 978-3-642-12766-3